Chemical Engineering Journal 381 (2020) 122735

Contents lists available at ScienceDirect

Chemical Engineering Journal

journal homepage: www.elsevier.com/locate/cej

Stabilizing $CsPbBr_3$ perovskite quantum dots on zirconium phosphate nanosheets through an ion exchange/surface adsorption strategy

Yang Li[a,b,1], Liubing Dong[c,1], Robert Patterson[b], Zhi Li Teh[b], Yicong Hu[b], Shujuan Huang[b,d,*], Chao Chen[a,*]

[a] College of Energy, Xiamen University, Xiamen 361005, China
[b] School of Photovoltaic and Renewable Energy Engineering, University of New South Wales, Sydney 2052, Australia
[c] Graduate School at Shenzhen, Tsinghua University, Shenzhen 518055, China
[d] School of Engineering, Macquarie University, Sydney 2109, Australia

HIGHLIGHTS

- An ion exchange/surface adsorption strategy was proposed to stabilize $CsPbBr_3$ PQDs.
- $CsPbBr_3$ PQDs were anchored on α-ZrP nanosheets.
- The $CsPbBr_3$ PQD/α-ZrP composite exhibited greatly enhanced stability.

GRAPHICAL ABSTRACT

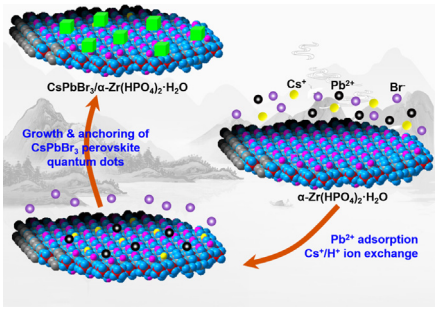

ARTICLE INFO

Keywords:
$CsPbBr_3$ perovskite quantum dots
Stability
Zirconium phosphate
LED
Display

ABSTRACT

All-inorganic perovskite quantum dots (PQDs) being characterized by high photoluminescence quantum yield, tunable emission colors and high color purity attract enormous attention in optoelectronic fields, especially as highly efficient narrow-band phosphors for lighting and next-generation display devices. However, poor stability seriously impedes their practical applications. Herein, we proposed an ion exchange/surface adsorption strategy to realize the room-temperature synthesis and stabilization of $CsPbBr_3$ PQDs on α-$Zr(HPO_4)_2{\cdot}H_2O$ (zirconium phosphate, α-ZrP) nanosheets. The inherent characteristics of the α-ZrP nanosheets including high Pb^{2+} adsorptivity and good Cs^+ ion exchange capability promoted the heterogeneous nucleation-growth and effective anchoring of $CsPbBr_3$ PQDs on α-ZrP surfaces. Consequently, the synthesized α-ZrP/$CsPbBr_3$ composite exhibited superior green-emitting performance and significantly enhanced humidity stability and thermal stability in comparison to pure PQDs and many other matrix-protected PQDs. All these favorable characteristics listed above endowed the α-ZrP/$CsPbBr_3$ composite with good optical properties for lighting and displays. This work opens up a new way to use inorganic nanomaterials to stabilize all-inorganic PQDs and can promote the scalable synthesis of PQDs with long-term stability for optoelectronic devices.

* Corresponding authors at: School of Photovoltaic and Renewable Energy Engineering, University of New South Wales, Sydney 2052, Australia (S. Huang). College of Energy, Xiamen University, Xiamen 361005, China (C. Chen).
E-mail addresses: sj.huang@unsw.edu.au (S. Huang), cchen@xmu.edu.cn (C. Chen).
[1] These two authors contributed equally to this work.

https://doi.org/10.1016/j.cej.2019.122735
Received 14 June 2019; Received in revised form 11 August 2019; Accepted 5 September 2019
Available online 06 September 2019
1385-8947/

1. Introduction

All-inorganic $CsPbX_3$ (X = Cl, Br, I) perovskite quantum dots (PQDs) with regulatable halide components, high photoluminescence quantum yield (PLQY), tunable emission colors and high color purity attract enormous attention in optoelectronic fields, especially as highly efficient narrow-band phosphors for lighting and next-generation display devices [1–7]. However, their poor chemical stability, *e.g.*, moisture sensitivity and thermal-induced degradation, hinders their practical applications for lighting and backlight displays [8–13]. For instance, when PQDs are utilized for light-emitting diodes (LEDs), lighting LEDs inevitably generate heat and cause the PQDs to be exposed to elevated temperatures. To stabilize $CsPbX_3$ PQDs, substantial efforts have been devoted, such as encapsulation using organic polymer matrices [14–16] or inorganic matrices [17–22]. Unfortunately, the protection offered by an organic polymer matrix is inadequate considering that many polymer matrices themselves cannot endure high temperatures. By contrast, inorganic matrices are generally stable at high temperatures, making it possible for them to improve the thermal stability of PQDs. Moreover, inorganic matrix-protected PQD composite powders have the advantage that they can be directly compatible with mature packaging techniques for commercial white LEDs [18,23]. To achieve better photoluminescence (PL) performance, surface design of inorganic matrices (*e.g.*, designing aminated surface for silica particles) was performed to guarantee the uniform size and good dispersion of PQDs [18,19]. The essence is that these inorganic matrix materials with well-designed surfaces provide abundant sites for PQDs' nucleation-growth and adsorption [19]. However, it is undeniable that the surface design of inorganic matrix materials increases the complexity of the synthesis processes of PQDs.

In recent years, inorganic nanosheet materials are widely studied for electrochemical energy storage, catalytic reactions, optoelectronic devices, *etc.*, benefiting from their unique micro-morphologies, relatively large specific surface area and subtle electronic structures [24–26]. This inspires us to explore the feasibility of utilizing inorganic nanosheets as a matrix to protect PQDs. Considering that appropriate interaction between matrix surface and PQDs is helpful to anchor PQDs and prevent PQDs' aggregation at high temperatures or in moist environments, seeking suitable inorganic nanosheet materials that can interact positively with PQDs and thus stabilize PQDs is highly desired, whereas the interfacial engineering of inorganic nanosheet-PQDs is a big challenge. Zirconium phosphate nanosheets, with the chemical formula of α-Zr$(HPO_4)_2{\cdot}H_2O$ (α-ZrP), own unique ion exchange/surface adsorption properties, typical layered structure and good heat stability, thus have been applied for sewage treatment, *etc* [27–29]. However, to our best knowledge, α-ZrP nanosheets have never been used to stabilize $CsPbBr_3$ PQDs.

Herein, we proposed an ion exchange/surface adsorption strategy to realize the room-temperature synthesis and stabilization of $CsPbBr_3$ PQDs on α-ZrP nanosheets (Fig. 1). This strategy was achieved based on the high Pb^{2+} adsorptivity and good Cs^+ ion exchange capability of α-ZrP nanosheets, which promoted the heterogeneous nucleation-growth and effective anchoring of $CsPbBr_3$ PQDs on the α-ZrP surfaces. The synthesized α-ZrP/$CsPbBr_3$ composite exhibited superior green-emitting behavior and significantly enhanced humidity and thermal stability, which endowed them with attractive performance in white LEDs and displays. This work provides an effective strategy using inorganic nanomaterial matrices for facile synthesis and stabilization of all-inorganic PQDs for optoelectronic devices.

2. Experimental

2.1. Chemicals and materials

All chemicals were used as received without further purification. Oleic acid (OA) and oleylamine (OAm) were purchased from Aladdin Reagent Co., Ltd. N, N-Dimethylformamide (DMF) and toluene were supplied by Sinopharm Chemical Reagent Co., Ltd. $PbBr_2$ (99.99%) and CsBr (99.9%) were obtained from Xi'an Polymer Light Technology Corp. α-ZrP was provided by Sunshine Technology Co., Ltd. The blue LED chip was obtained from EPI LEDs Co., Ltd. Commercial phosphors of (Sr,Ca)$AlSiN_3$:Eu^{2+}, K_2SiF_6:Mn^{4+} (*i.e.*, KSF) and $(Sr,Ba)_2SiO_4$:Eu^{2+} were purchased from Shenzhen Looking Long Technology Co., Ltd.

2.2. Synthesis of α-ZrP/$CsPbBr_3$ composite powder

0.4 mmol of $PbBr_2$ and 0.4 mmol of CsBr were dissolved in DMF (10 mL) while stirring, then 1 mL of OA and 0.5 mL of OAm were added as ligands to form a precursor solution. Separately, 0.2 g α-ZrP powder was dispersed in 10 mL of toluene under stirring. Subsequently, 1 mL of the above precursor solution was added to the α-ZrP/toluene system under stirring for 1 min at room temperature and then left to stand for 30 min. The produced powder was collected at the bottom of the beaker, washed with hexane and naturally dried in the air to get an α-ZrP/$CsPbBr_3$ PQD composite.

2.3. Assembly of α-ZrP/$CsPbBr_3$ LEDs

Two kinds of white LEDs were assembled with the synthesized α-ZrP/$CsPbBr_3$ composite powder, a blue InGaN chip and a commercial red phosphor of (Sr,Ca)$AlSiN_3$:Eu^{2+} or KSF. In detail, the red phosphors and the α-ZrP/$CsPbBr_3$ composite powder were mixed with silicone thoroughly to form a hybrid sol and then dropped onto the blue-emitting InGaN chip. Also, a green LED was constructed by spreading the α-ZrP/$CsPbBr_3$ composite powder on a blue InGaN chip.

2.4. Characterization

X-ray diffraction (XRD) analyzer (model: Ultima-IV) with a Cu Kα radiation was used to analyze the crystal structure of samples. Valence states of elements in the α-ZrP/$CsPbBr_3$ composite were detected by X-ray photoelectron spectroscopy (XPS; model: PHI Quantum-2000). The

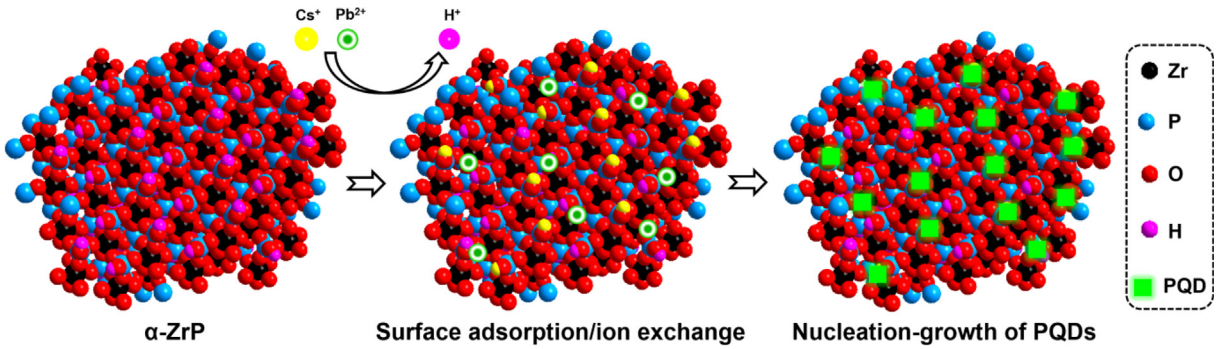

Fig. 1. Schematic illustration for the synthesis of $CsPbBr_3$ PQDs on α-ZrP nanosheets.

microscopic-morphologies of the samples were observed using field emission scanning electron microscopy (SEM; model: SUPRA 55) and high-resolution transmission electron microscopy (TEM; model: FEI Tecnai G2 F30). Fourier transform infrared spectroscopy (FTIR) analysis was carried out using a spectrometer (model: Nicolet iS5). Thermogravimetric (TG) measurements and N_2 adsorption/desorption tests were performed on a simultaneous thermal analyzer (model: Netzsch STA 449 F5 Jupiter) and a Brunauer-Emmett-Teller (BET) analyzer (model: ASAP 2020M + C), respectively. PL emission spectra and PLQY tests were carried out on a fluorescence spectrophotometer equipped with visible and near-infrared photomultiplier tube detectors (model: FLS980, Edinburgh Instruments). The humidity stability of the α-ZrP/$CsPbBr_3$ composite was examined by keeping it in a moist environment (room temperature with ~80% humidity) and its PL emission spectra were recorded every few hours. A charge-coupled device (model: Ocean Optics, USB2000 +) and a cooling/heating stage (model: Linkam Scientific Instruments, THMS600E) were used to record temperature-dependent PL spectra (temperature range: 0–100 °C). The electroluminescence (EL) spectra, luminous efficacy, correlated color temperature (CCT), color-rendering index (CRI), Commission International De L'Eclairage (CIE) and color purity of these LEDs were analyzed using an integrating sphere (HAAS-2000, Everfine, China).

3. Results and discussion

As-received α-ZrP is a white powder with a nanosheet-like micro-morphology and lateral dimension of 1–4 μm (Fig. 2a). Most of the α-ZrP sheets possess a thickness of less than 100 nm as shown in Fig. S1. N_2 adsorption-desorption isotherms in Fig. S2 show that the α-ZrP sample is a typical mesoporous material. Besides, the α-ZrP raw-material has high crystallinity, reflected by the sharp diffraction peaks at 11.7°, 19.8°, 24.9°, 33.8° and so on in the XRD pattern (Fig. 2b), correspond well to the α-ZrP phase (PDF#34-0127). More importantly, α-ZrP possesses a layered crystal structure and massive hydroxyl (–OH) groups on the surface (as illustrated in Fig. 2c), and has been widely used for waste water treatment and catalytic reactions, benefiting from its good ion exchange ability and high Pb^{2+} adsorptivity [30-33]. Especially, surface ion exchange between monovalent Cs^+ and H^+ on the α-ZrP surface is easy to happen [31], although large radius makes Cs^+ cations hard to directly intercalate into α-ZrP (note that ion exchange between Pb^{2+} and α-ZrP through an intercalation process is also possible, but corresponding kinetics is relatively slow) [32]. The acidity of the hydrogen atoms that are bound to anionic HPO_4^{2-} groups is very low, and they are readily exchanged for other cations such as Cs^+ [32,34]. This can be considered as the driving force for surface ion exchange between Cs^+ and H^+ on the α-ZrP surface. In order to verify the surface ion exchange behavior between monovalent Cs^+ and H^+ on the α-ZrP surface, we immersed α-ZrP powder in CsBr/DMF solution for 1–2 min and then washed for several times. SEM image, EDS mapping and XPS spectra of the treated powder are given in Fig. 2d and Fig. S3. The detected Cs element confirms the surface ion exchange between Cs^+ and H^+ on the α-ZrP surface. Remarkably, the surface ion exchange behavior between Cs^+ and H^+ will be very useful for anchoring $CsPbBr_3$ PQDs on the surface of α-ZrP nanosheets during the synthesis process of the α-ZrP/$CsPbBr_3$ PQD composite.

For the synthesized α-ZrP/$CsPbBr_3$ PQD composite, it has a similar micro-morphology compared to the pristine α-ZrP nanosheets (Fig. 3a and Fig. S1), while EDS mapping result in Fig. 3b reveals a uniform distribution of PQDs in the composite. Also, the PQDs are directly observed on the surface of the α-ZrP nanosheets from the high-resolution TEM image in Fig. 3c: the PQDs have a size of about 4–7 nm and the fringe spacing is measured to be 0.24 nm consistent to the index of (2 1 1) crystal plane of cubic $CsPbBr_3$ PQDs. The XRD pattern of the α-ZrP/$CsPbBr_3$ PQD composite powder is displayed in Fig. 3d. Due to the very small size of the $CsPbBr_3$ PQDs (as discussed in Fig. 3c), and being enveloped by the α-ZrP nanosheets, characteristic diffraction peaks of $CsPbBr_3$ PQDs are relatively weak [35,36]. Despite this, the diffraction peaks at $2\theta = 30.6°$, *etc.*, can be indexed to cubic $CsPbBr_3$ PQDs

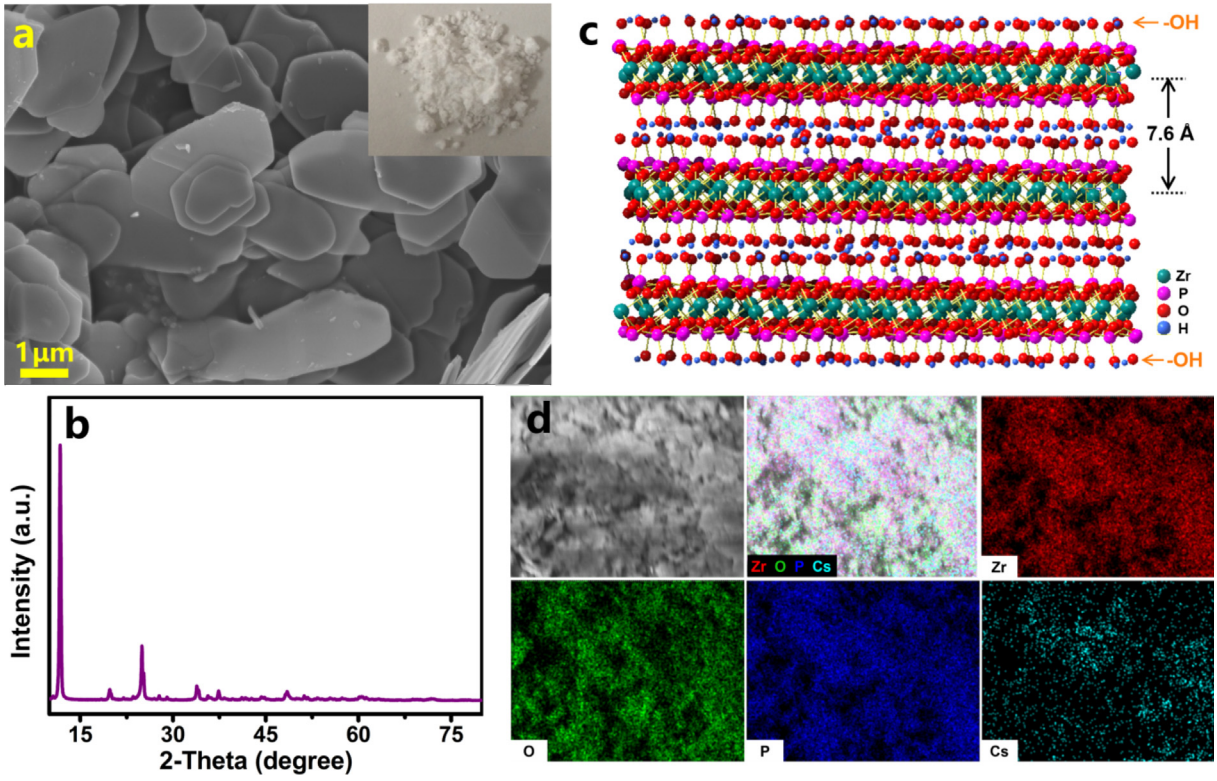

Fig. 2. (a) SEM image (inset: photograph) and (b) XRD pattern of the as-received α-ZrP powder. (c) Schematic illustration of α-ZrP crystal structure. (d) EDS mapping of the α-ZrP powder after surface ion exchange with Cs^+.

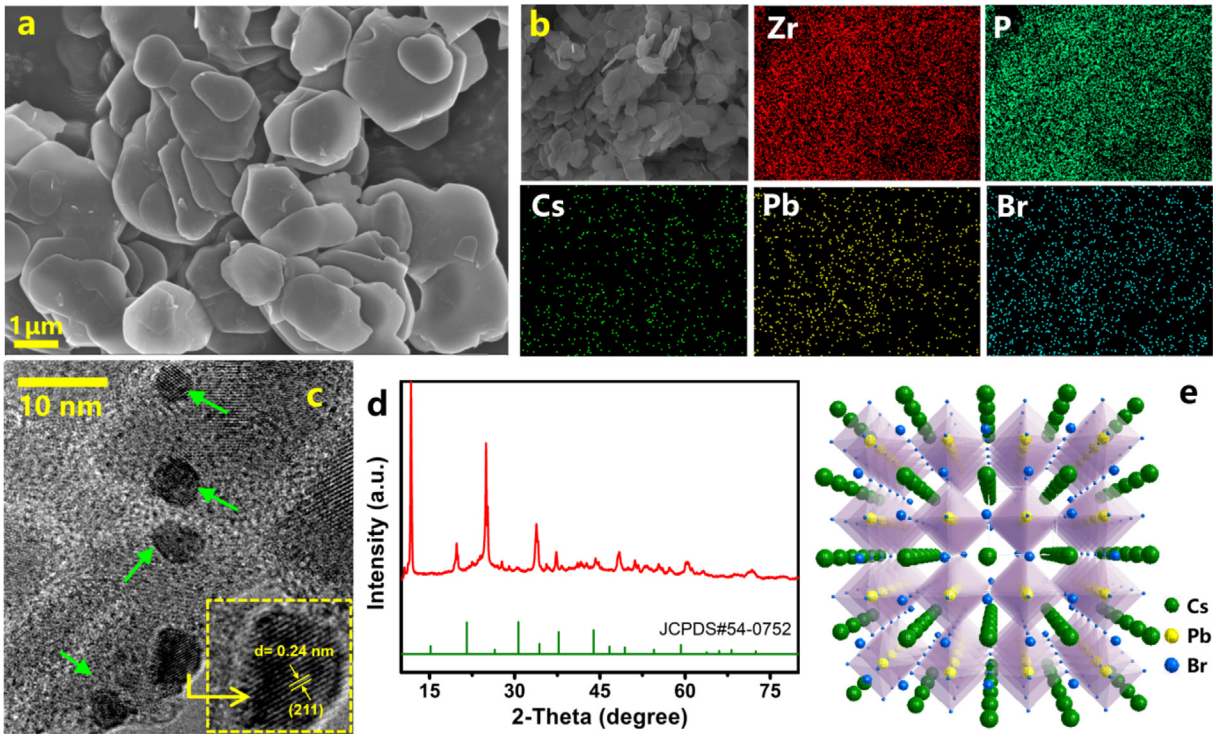

Fig. 3. (a) SEM image, (b) EDS mapping (with the analysis area of ~400 μm^2), (c) high-resolution TEM images (the particles pointed out by green arrows are $CsPbBr_3$ PQDs and inset shows the particles' lattice fringes) and (d) XRD pattern of the α-ZrP/$CsPbBr_3$ PQD composite powder. (e) Crystal structure of cubic $CsPbBr_3$ PQDs. (For interpretation of the references to color in this figure legend, the reader is referred to the web version of this article.)

(PDF#54-0752; as illustrated in Fig. 3e).

To comprehensively investigate the α-ZrP/$CsPbBr_3$ PQD composite, XPS, FTIR spectroscopy and TG analysis were performed. In the XPS full spectrum of the α-ZrP/$CsPbBr_3$ PQD composite powder (Fig. 4a), the signals related to Zr, P, O, Cs, Pb, and Br elements are detected. In detail, XPS fine spectra in Fig. 4b–d suggest that binding energies of Cs $3d_{5/2}$ (723.8 eV), Cs $3d_{3/2}$ (737.9 eV), Pb $4f_{7/2}$ (138.4 eV), Pb $4f_{5/2}$ (143.2 eV), Br $3d_{5/2}$ (68.2 eV) and Br $3d_{3/2}$ (69.3 eV) are close to the values for $CsPbBr_3$ PQDs that have been reported in the literature, further confirming the formation of $CsPbBr_3$ PQDs in the α-ZrP/$CsPbBr_3$ PQD composite powder [14,22,37]. Note that anchoring of PQDs on the α-ZrP nanosheets inevitably affects the binding energies of

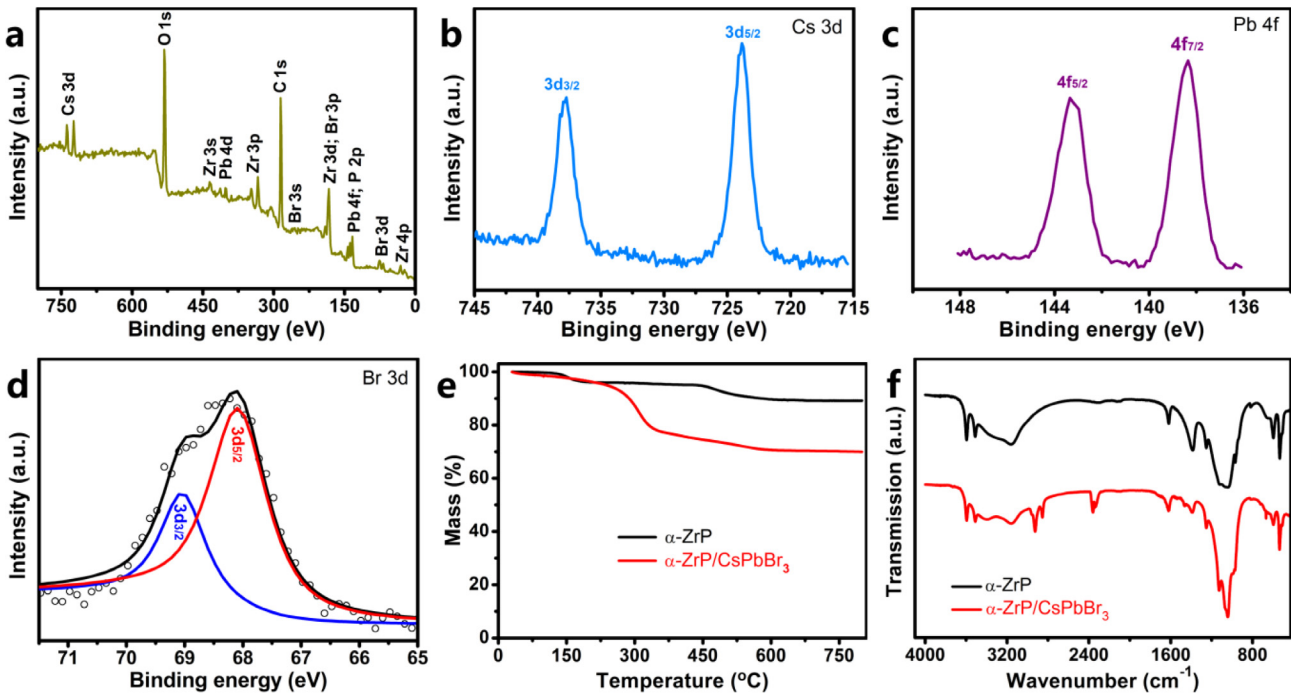

Fig. 4. (a–d) XPS spectra, (e) TG curve and (f) FTIR spectrum of the α-ZrP/$CsPbBr_3$ composite powder. (a), (b), (c) and (d) are XPS full spectrum, Cs 3d spectrum, Pb 4f spectrum and Br 3d spectrum, respectively. TG curve and FTIR spectrum of α-ZrP are provided in (e) and (f), respectively.

Cs 3d, Pb 4f, and Br 3d to some extent. Apart from PQDs and α-ZrP, possibly preserved organic components (*e.g.*, DMF, OA and OAm) in the synthesized composite powder were studied. From the TG curve of the pure α-ZrP in Fig. 4e, we can see that α-ZrP is stable before 120 °C and then two weight loss sections appear. The weight loss in the temperature range of 120–210 °C and 430–650 °C is associated with the removal of H_2O from the monohydrate α-ZrP and the process that phosphate groups condense to zirconium pyrophosphate [38], respectively. For the α-ZrP/$CsPbBr_3$ composite sample, it shows an additional mass loss in the temperature of 210–430 °C. This proves the existence of OA and OAm in the composite because boiling points of the two ligands are in such a temperature range. As shown in Fig. 4f, the FTIR spectrum of the α-ZrP contains an intense characteristic peak at 1050 cm^{-1}, originating from the P-O stretching vibration of interlayer PO_4 groups. The broad adsorption bands at 3590, 3510, 3150 and 1618 cm^{-1} can be ascribed to the OH stretching vibration of α-ZrP [39–41]. For the α-ZrP/$CsPbBr_3$ composite, some other adsorption bands are observed. The adsorption band at 3305 cm^{-1} is an NH stretching mode, indicating the presence of OAm [42]. Typical absorption band for the species with hydrocarbon groups is detected at 2935 cm^{-1}, and two asymmetric vibrations with one symmetric stretching vibration of the carboxylate group are also found at 1520 and 1410 cm^{-1}. These bands are considered to be from OA [43,44]. In short, TG and FTIR results prove the presence of OA and OAm in the α-ZrP/$CsPbBr_3$ PQD composite. It is considered that the two hydrophobic ligands (*i.e.*, OA and OAm) can help to control PQDs' size, prevent PQD aggregation and enhance PQDs' stability [9,45].

The above discussions clearly demonstrate the presence of $CsPbBr_3$ PQDs on the α-ZrP nanosheets. It is equally necessary to probe into the formation process of the PQDs and their interaction with the α-ZrP nanosheets. As mentioned above, α-ZrP possesses a good ion exchange ability and high Pb^{2+} adsorptivity [30–33]. Therefore, during the synthesis of the α-ZrP/$CsPbBr_3$ composite, when CsBr-$PbBr_2$-DMF precursor was mixed with the α-ZrP/toluene suspension, Cs^+ and Pb^{2+} would be adsorbed onto the surface of the α-ZrP nanosheets, accompanied by a surface ion exchange between some Cs^+ and the α-ZrP (Fig. 2d and Fig. S3), and then $CsPbBr_3$ PQDs nucleated and grew up around these Pb^{2+} and Cs^+ that located on the α-ZrP surfaces (as illustrated in Fig. 1. Note that some PQDs would spontaneously form in the solution, instead of on α-ZrP nanosheet surfaces, while these PQDs were removed during the washing process with hexane). Obviously, such a formation process benefits to the strong anchoring of the PQDs on the α-ZrP nanosheets. Evidence of this strong anchoring is that the PQDs were not observed to fall off from the α-ZrP even the synthesized α-ZrP/$CsPbBr_3$ composite powder was mixed with hexane and then shook vigorously (Fig. S4).

Luminescence properties of the synthesized α-ZrP/$CsPbBr_3$ composite are then investigated. The α-ZrP/$CsPbBr_3$ sample is a yellow powder, which exhibits intense green emission under irradiation from a UV (365 nm) light (inset in Fig. 5a). In its PL spectrum under an excitation wavelength of 450 nm, a highly symmetric emission peak centered at ~517 nm and a narrow full width at half maximum (FWHM) of 23 nm under an excitation wavelength of 450 nm are observed (Fig. 5a), indicating good green-emitting performance of the composite. The FWHM of the α-ZrP/$CsPbBr_3$ composite is much narrower than that of commercial phosphors (Fig. S5), which is essential to obtain high color purity for display applications. Meanwhile, a PLQY of 50% is achieved (Fig. S6). This value is notably higher than the figures for previously reported pure $CsPbBr_3$ PQDs (with a low PLQY of 6%), ethyl cellulose/$CsPbBr_3$ PQD composite films (PLQY of 37%) and glass protected $CsPbBr_3$ PQDs (PLQY of 42%) [15,21,46]. This high PLQY is comparable to that of natural mineral halloysite nanotube/PQDs, aminated SiO_2 particles/PQDs and mesoporous metal-organic frameworks/PQDs that were synthesized at high temperatures [19,21,35]. For pure PQDs in the solid state, ligands are easy to detach from their surface. As a result, surface defects form and PQD particles aggregate in air, leading to a low PLQY [47]. While for the ethyl cellulose/$CsPbBr_3$ PQD composite film [15], the PQDs were synthesized firstly and then hybridized with ethyl cellulose. Obviously, the PQDs were not under protection before hybridizing with the ethyl cellulose film. Meanwhile, during the polymerization of the composite film, the PQDs may aggregate and grow into large nanocrystals. By contrast, for the α-ZrP/$CsPbBr_3$ PQDs composite, natural mineral halloysite nanotube/PQDs, aminated SiO_2 particles/PQDs and mesoporous metal-organic frameworks/PQDs [19,21,35], PQDs were *in-situ* grew on the surfaces of these inorganic materials and exhibited a small size. Besides, these inorganic matrices could also passivate the PQDs [20,48,49]. Consequently, these composites were endowed with higher PLQY values. In addition, a green LED constructed using the α-ZrP/$CsPbBr_3$ composite powder and a blue InGaN chip also confirms the composite's outstanding green-emitting performance with CIE chromaticity coordinate of (0.164, 0.772) and high color purity of 92% (Fig. 5b and Fig. S7).

The lead halide perovskite nanocrystal structure of $CsPbBr_3$ PQDs with ionic nature tends to degrade when $CsPbBr_3$ PQDs contact a moist environment [50,51]. They are also easy to aggregate when the PQDs are exposed to relatively high temperatures (it is considered that thermal-induced PL quenching mainly arises from the degradation and agglomeration of PQDs [20,22]). That is, PQDs possess poor humidity stability and thermal stability, inevitably leading to modest performance of PQDs-based optoelectronic devices. Therefore, how to enhance humidity stability and thermal stability of $CsPbBr_3$ PQDs is a critical issue for their practical applications. It is inspiring to find that our α-ZrP/$CsPbBr_3$ composite shows excellent humidity stability: its PL intensity declines only ~16% of its initial intensity after exposure to the humid environment for ~640 h (Fig. 6a). Such humidity stability is much better than that of pure $CsPbBr_3$ PQDs and some other inorganic matrices (*e.g.*, CaF_2 and *h*-BN nanosheets) protected $CsPbBr_3$ PQDs [20,22], showing the prominent advantage of using α-ZrP nanosheets to stabilize PQDs. As pointed by Huang et al. [52], moisture-induced degradation of PQDs is always accompanied by the increased size of PQD nanocrystals. In our α-ZrP/$CsPbBr_3$ composite, the $CsPbBr_3$ PQDs are anchored on the surface of the α-ZrP nanosheets. Meanwhile, the "wall-like" α-ZrP nanosheets separate the PQDs (as illustrated in Fig. S8). Therefore, PQDs' movement and regrowth into large crystals are suppressed. This mechanism has also been confirmed in other inorganic materials protected PQDs [19,22]. At the same time, the remaining OA and OAm ligands in the composite serve as a water-resisting layer and contribute to the enhancement of the PQDs' humidity stability [9,45]. Besides, even after 7 months since the synthesis of the α-ZrP/$CsPbBr_3$ composite (note that the composite was stored in air with a humidity of 30–60% during the 7 months), the composite powder exhibits intense green emission under UV light (inset in Fig. 6a), and its PLQY retention is about 50%. Serious aggregation of PQDs is not observed in the TEM and high-resolution TEM images of the α-ZrP/$CsPbBr_3$ composite after 7-month storage (Fig. S9). These suggest that the α-ZrP/$CsPbBr_3$ composite has a relatively good long-term storage stability.

Moreover, the thermal stability of the PQDs is also improved by hybridizing with the α-ZrP nanosheets. We can intuitively see from Fig. 6b and Fig. S10 that during a heating-cooling process (*i.e.* the temperature was raised from 0 to 100 °C and then cooled down to 0 °C), the PL intensity of the α-ZrP/$CsPbBr_3$ composite decreases with increasing temperature and then increases with decreasing temperature, and finally, the PL intensity recovers up to 94% of its initial value (Fig. 6c). By contrast, the PL intensity of pure $CsPbBr_3$ PQDs only retained 35% of its original intensity when the temperature increased from room temperature to 100 °C and then decreased to the room temperature (inset in Fig. 6c) [48]. Furthermore, during repeated heating-cooling processes, the α-ZrP/$CsPbBr_3$ composite also exhibits high PL recovery ability (Fig. S11). The excellent thermal stability of the α-ZrP/$CsPbBr_3$ composite can be attributed to several reasons: (i) outstanding thermal stability of α-ZrP itself is essential to protect $CsPbBr_3$ PQDs under high temperature [53,54]; (ii) the PQDs are anchored on the α-ZrP nanosheets and the "wall-like" α-ZrP nanosheets

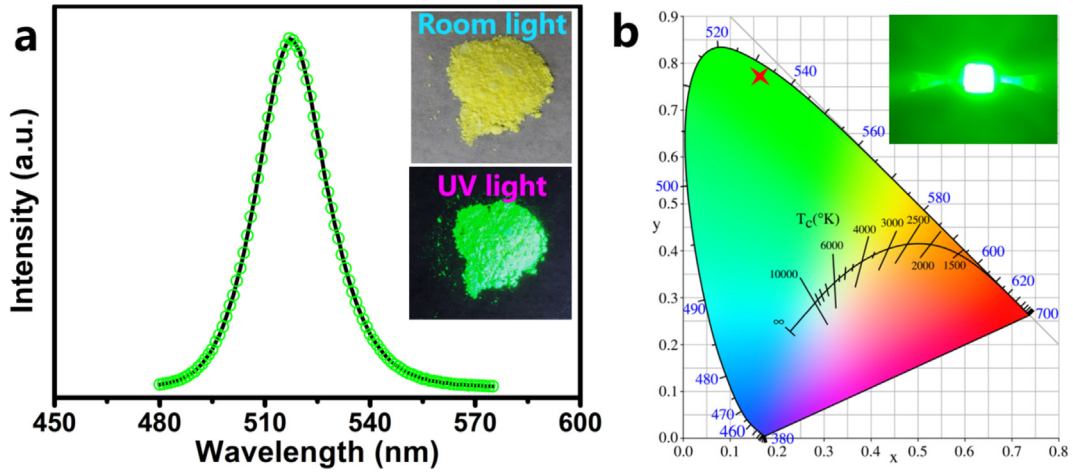

Fig. 5. (a) PL emission spectrum and photographs (insets) of the α-ZrP/$CsPbBr_3$ composite powder. (b) CIE chromaticity diagram of the green-emitting LED constructed by the α-ZrP/$CsPbBr_3$ PQD composite and a blue InGaN chip (inset: photograph of the lighting green-emitting LED). (For interpretation of the references to color in this figure legend, the reader is referred to the web version of this article.)

separate the PQDs from each other (Fig. S8), making the PQDs hard to regrow into large crystals when the α-ZrP/$CsPbBr_3$ composite is exposed to high temperatures (as confirmed by TEM observations of the α-ZrP/$CsPbBr_3$ composite before and after heat treatment in Fig. S9) [20,48,55]; (iii) high temperatures would accelerate moisture-induced decomposition of PQDs [56], while our α-ZrP/$CsPbBr_3$ composite possesses a superior humidity stability, thus the negative effects of high temperature will be alleviated. Additionally, the α-ZrP/$CsPbBr_3$ composite also exhibits a relatively good photo-stability, with 88% PL intensity retention after 36 h light irradiation (Fig. S12).

The optical properties of the α-ZrP/$CsPbBr_3$ composite for white LEDs and display applications are further studied. A white LED was constructed with the green-emitting α-ZrP/$CsPbBr_3$ composite powder, a commercial red phosphor of (Sr,Ca)$AlSiN_3$:Eu^{2+} and a blue-emitting InGaN chip. Fig. 7a presents the EL spectrum of the assembled white LED at a driving current of 20 mA (inset is a photograph of the LED emitting bright white light). The emission wavelengths of the (Sr,Ca)$AlSiN_3$:Eu^{2+}, α-ZrP/$CsPbBr_3$ composite and blue chip are 624, 521 and 456 nm, respectively. The coordinate value of the white LED is (0.395, 0.390) (CIE chromaticity diagram is given in Fig. 7b) with a luminous efficacy of 41 lm/W, a relatively low CCT of 3725 K and a CRI of 68. Compared with other white LEDs in Table 1, we can see that our reported luminous efficiency is at the middle level. The luminous efficiency value is promising to be further improved by various approaches, such as optimizing encapsulation process, changing phosphor ratio, reducing light scattering and increasing chip efficiency, *etc.*, which needs more research in our future work. As displayed in Fig. S13, the EL intensity of our assembled white LED only shows a small degradation after continuous lighting for 540 min. This also suggests that the synthesized α-ZrP/$CsPbBr_3$ composite powder has good stability. Furthermore, to evaluate the potential application of the α-ZrP/$CsPbBr_3$ composite for backlight display, a white LED based on the α-ZrP/$CsPbBr_3$ composite, a blue InGaN chip and a red KSF phosphor (with narrow emission peak, thus is suitable for displays; Fig. S14) was assembled, and its EL spectrum is shown in Fig. 7c. The CIE color coordinate of the white LED (*i.e.*, color gamut) covers 125% of the National Television System Committee (NTSC) standard (Fig. 7d), which is superior to that of previously reported white LEDs with phosphors, PQDs and Cd-based quantum dots, as summarized in Table S1. These results prove that the α-ZrP/$CsPbBr_3$ composite has potential applications in lighting and displays.

4. Conclusions

An ion exchange/surface adsorption strategy was developed to realize the room-temperature synthesis and stabilization of $CsPbBr_3$ PQDs on α-ZrP nanosheets. The high Pb^{2+} adsorptivity and good Cs^+ ion exchange capability of α-ZrP nanosheets promoted the heterogeneous nucleation-growth and effective anchoring of $CsPbBr_3$ PQDs on the surface of the α-ZrP nanosheets. As a result, the synthesized α-ZrP/$CsPbBr_3$ PQDs composite displayed good green-emitting performance with long-term humidity stability and excellent thermal stability. Assembled white LEDs based on the α-ZrP/$CsPbBr_3$ composite exhibited a low CCT and high luminous efficacy. Besides, the color gamut

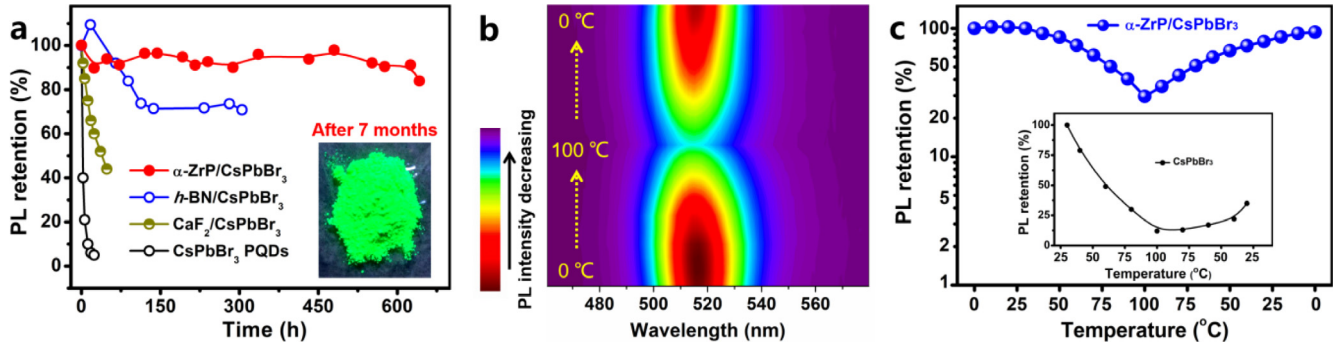

Fig. 6. (a) Humidity stability of the α-ZrP/$CsPbBr_3$ composite (inset: photograph under a UV light of the α-ZrP/$CsPbBr_3$ composite after 7 months since synthesis). Thermal stability of the α-ZrP/$CsPbBr_3$ composite: (b) PL intensity contour map and (c) summarized PL retention with the change of temperature. For comparison, humidity stability of $CsPbBr_3$ PQDs (ref. 20), CaF_2/$CsPbBr_3$ (ref. 20) and *h*-BN/$CsPbBr_3$ (ref. 22) and thermal stability of $CsPbBr_3$ PQDs (ref. 48) are listed in (a) and (c).

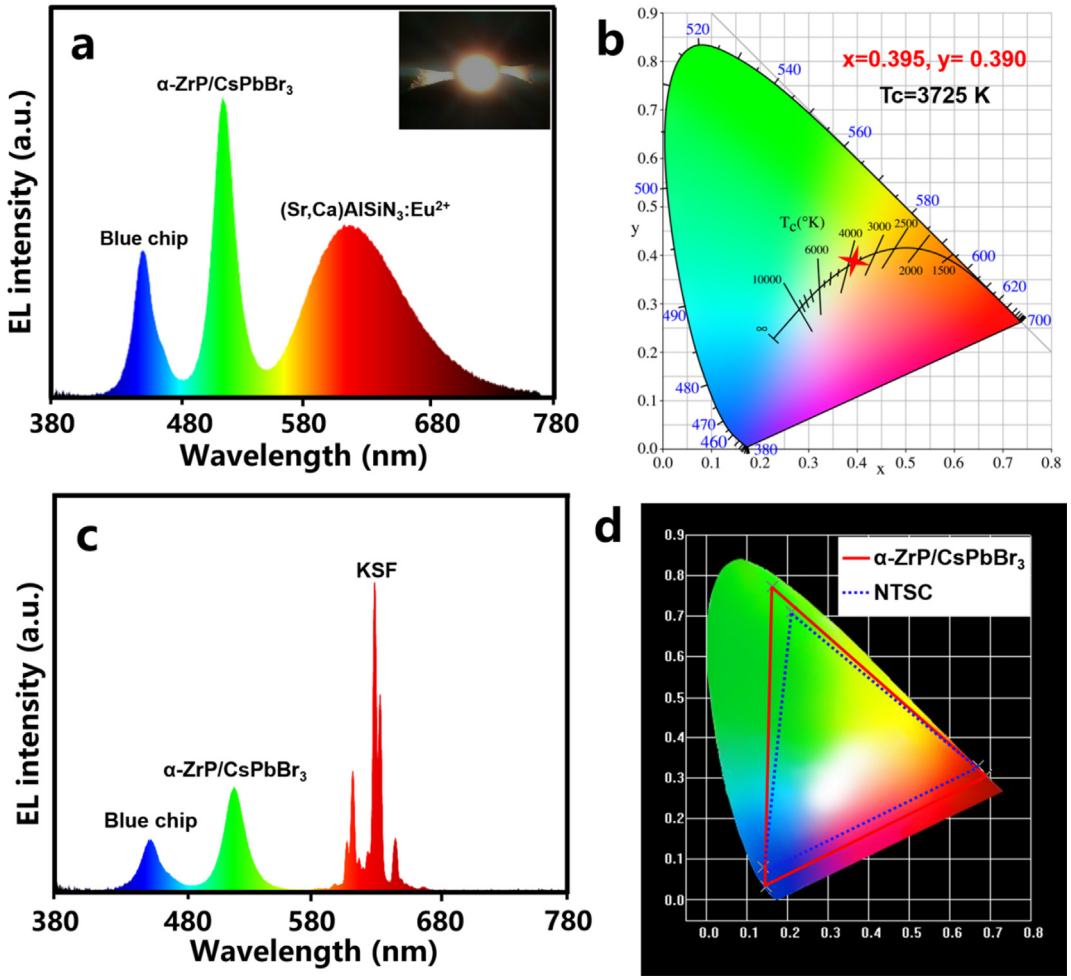

Fig. 7. (a) EL spectrum (inset: photograph of the lighting LED) and (b) CIE chromaticity diagram of the white LED constructed by the α-ZrP/$CsPbBr_3$ composite, (Sr,Ca)$AlSiN_3$:Eu^{2+} and a blue-emitting InGaN chip. (c) EL spectrum and (d) color gamut of the white LED constructed by the α-ZrP/$CsPbBr_3$ composite, a red KSF phosphor and a blue InGaN chip. (For interpretation of the references to color in this figure legend, the reader is referred to the web version of this article.)

of the white LEDs based on a blue InGaN chip, the green-emitting α-ZrP/$CsPbBr_3$ composite and a red-emitting KSF phosphor was 125% of the NTSC standard. Overall, the synthesis and stabilization of the $CsPbBr_3$ PQDs on the α-ZrP nanosheets were realized based on the inherent characteristics of the α-ZrP, avoiding additional surface modification process. We would like to mention that many other inorganic materials that own ion exchange/adsorption properties with Cs^+/Pb^{2+} or a layered structure, such as $Sn(HPO_4)_2{\cdot}H_2O$, $Ti(HPO_4)_2{\cdot}H_2O$, mesoporous titanium phosphates and so on [27,63–65], can be used to stabilize PQDs in theory. But to achieve good photoluminescence performance, optical property and chemical stability of these inorganic nanomaterials need to be considered [49,62]. For instance, the inorganic nanomaterials should have a large bandgap and not absorb the light emitted by PQDs. Above all, this work opens up a new way to use inorganic nanomaterials to stabilize all-inorganic PQDs and can promote the scalable synthesis of long-term stable PQDs for optoelectronic devices.

Acknowledgement

Y. Li would like to thank the financial support from Chinese Scholarship Council (Grant No. 201806310048).

Table 1
Comparison of the optical performance of various white LEDs.

Blue part	Green part	Red part	CCT (K)	CRI	Luminous efficacy (lm/W)	Refs.
Blue LED chip	α-ZrP/$CsPbBr_3$	(Sr,Ca)$AlSiN_3$:Eu^{2+}	3725	68	41	This work
Blue LED chip	$CsPbBr_3$/EVA	(Sr,Ca)$AlSiN_3$:Eu^{2+}	2347	75	38	[14]
Blue LED chip	$CsPb_{1-x}Sn_xBr_3$	$CaAlSiN_3$:Eu^{2+}	3128	74	29	[57]
Blue LED chip	$CsPbBr_3$/Cs_2GeF_6:Mn^{4+}		–	81	27	[36]
Blue LED chip	$CsPbBr_3$	K_2SiF_6:Mn^{4+}	4754	85	46	[58]
Blue LED chip	$CsPbBr_3$-SiO_2	$Sr_2Si_5N_8$:Eu^{2+}	5318	72	48	[59]
Blue LED chip	$CsPbBr_3$-SiO_2	K_2SiF_6:Mn^{4+}	7425	83	64	[60]
Blue LED chip	CaF_2-$CsPbBr_3$	K_2SiF_6:Mn^{4+}	–	63	–	[20]
Blue LED chip	$CsPbBr_3$/glass	$CaAlSiN_3$:Eu^{2+}	3674	83	51	[46]
Blue LED chip	$CsPbBr_3$: Na^+	K_2SiF_6:Mn^{4+}	6652	75	67	[61]
UV-chip	$CsPbBr_3$	$CsPbMnCl_3$@SiO_2	3950	82	78	[62]

Appendix A. Supplementary data

Supplementary data to this article can be found online at https://doi.org/10.1016/j.cej.2019.122735.

References

[1] L. Protesescu, S. Yakunin, M.I. Bodnarchuk, F. Krieg, R. Caputo, C.H. Hendon, R.X. Yang, A. Walsh, M.V. Kovalenko, Nano Lett. 15 (2015) 3692.
[2] J. Zhou, Z. Hu, L. Zhang, Y. Zhu, J. Alloys Compd. 708 (2017) 517.
[3] M. Zhang, M. Wang, Z. Yang, J. Li, H. Qiu, J. Alloys Compd. 748 (2018) 537.
[4] K. Huang, D. Li, L. Yang, S. Liu, F. Yang, J. Alloys Compd. 710 (2017) 244.
[5] Z. Li, L. Kong, S. Huang, L. Li, Angew. Chem. 129 (2017) 8246.
[6] C. Li, Z. Zang, W. Chen, Z. Hu, X. Tang, W. Hu, K. Sun, X. Liu, W. Chen, Opt. Express 24 (2016) 15071.
[7] Z. Shi, S. Li, Y. Li, H. Ji, X. Li, D. Wu, T. Xu, Y. Chen, Y. Tian, Y. Zhang, C. Shan, G. Du, ACS Nano 12 (2018) 1462.
[8] P. Vashishtha, J.E. Halpert, Chem. Mater. 29 (2017) 5965.
[9] C. Sun, Y. Zhang, C. Ruan, C. Yin, X. Wang, Y. Wang, W.W. Yu, Adv. Mater. 28 (2016) 10088.
[10] J. Pan, L.N. Quan, Y. Zhao, W. Peng, B. Murali, S.P. Sarmah, M. Yuan, L. Sinatra, N.M. Alyami, J. Liu, E. Yassitepe, Z. Yang, O. Voznyy, R. Comin, M.N. Hedhili, O.F. Mohammed, Z.H. Lu, D.H. Kim, E.H. Sargent, O.M. Bakr, Adv. Mater. 28 (2016) 8718.
[11] Z. Shi, Y. Li, Y. Zhang, Y. Chen, X. Li, D. Wu, T. Xu, C. Shan, G. Du, Nano Lett. 17 (2017) 313.
[12] W. Chen, X. Tang, P. Wangyang, Z. Yao, D. Zhou, F. Chen, S. Li, H. Lin, F. Zeng, D. Wu, K. Sun, M. Li, Y. Huang, W. Hu, Z. Zang, J. Du, Adv. Opt. Mater. 6 (2018) 1800007.
[13] D. Yan, T. Shi, Z. Zang, T. Zhou, Z. Liu, Z. Zhang, J. Du, Y. Leng, X. Tang, Small 15 (2019) 1901173.
[14] Y. Li, Y. Lv, Z. Guo, L. Dong, J. Zheng, C. Chai, N. Chen, Y. Lu, C. Chen, A.C.S. Appl, Mater. Interfaces 10 (2018) 15888.
[15] Y.H. Song, J.S. Yoo, B.K. Kang, S.H. Choi, E.K. Ji, H.S. Jung, D.H. Yoon, Nanoscale 8 (2016) 19523.
[16] H. Zhang, X. Wang, Q. Liao, Z. Xu, H. Li, L. Zheng, H. Fu, Adv. Funct. Mater. (2017) 1604382.
[17] J.Y. Sun, F.T. Rabouw, X.F. Yang, X.Y. Huang, X.P. Jing, S. Ye, Q.Y. Zhang, Adv. Funct. Mater. 27 (2017) 1704371.
[18] H.C. Wang, S.Y. Lin, A.C. Tang, B.P. Singh, H.C. Tong, C.Y. Chen, Y.C. Lee, T.L. Tsai, R.S. Liu, Angew. Chem. Int. Ed. 55 (2016) 7924.
[19] X. Li, Y. Wang, H. Sun, H. Zeng, Adv. Mater. 29 (2017) 1701185.
[20] Y. Wei, H. Xiao, Z. Xie, S. Liang, S. Liang, X. Cai, S. Huang, A.A. Al Kheraif, H.S. Jang, Z. Cheng, J. Lin, Adv. Opt. Mater. 6 (2018) 1701343.
[21] J. Hao, X. Qu, L. Qiu, G. Li, Y. Wei, G. Xing, H. Wang, C. Yan, H.S. Jang, Z. Cheng, J. Lin, Adv. Opt. Mater. (2018) 1801323.
[22] Y. Li, L. Dong, N. Chen, Z. Guo, Y. Lv, J. Zheng, C. Chen, A.C.S. Appl, Mater. Interfaces 11 (2019) 8242.
[23] S. Ye, F. Xiao, Y.X. Pan, Y.Y. Ma, Q.Y. Zhang, Mater. Sci. Eng. R 71 (2010) 1.
[24] Y. Guo, K. Xu, C. Wu, J. Zhao, Y. Xie, Chem. Soc. Rev. 44 (2015) 637.
[25] H. Xia, Q. Xu, J. Zhang, Nano-Micro Lett. 10 (2018) 66.
[26] Y. Zhu, L. Peng, Z. Fang, C. Yan, X. Zhang, G. Yu, Adv. Mater. 30 (2018) 1706347.
[27] A. Clearfield, J.A. Stynes, J. Inorg. Nucl. Chem. 26 (1964) 117.
[28] A. Clearfield, Chem. Rev. 88 (1988) 125.
[29] R.M. Kim, J.E. Pillion, D.A. Burwell, J.T. Groves, M.E. Thompson, Inorg. Chem. 32 (1993) 4509.
[30] L. Wang, W.H. Xu, R. Yang, T. Zhou, D. Hou, X. Zheng, J.H. Liu, X.J. Huang, Anal. Chem. 85 (2013) 3984.
[31] G. Alberti, M. Casciola, U. Costantino, G. Levi, G. Ricciardi, J. Inorg. Nucl. Chem. 40 (1978) 533.
[32] J. Sanchez, M.V. Ramos-Garcés, I. Narkeviciute, J.L. Colón, T.F. Jaramillo, Catalysts 7 (2017) 132.
[33] H. Xiao, S. Liu, Mater. Des. 155 (2018) 19.
[34] K. Dorfner, Ion Exchangers, Walters de Gruyter, Berlin, 1991.
[35] J. Ren, T. Li, X. Zhou, X. Dong, A.V. Shorokhov, M.B. Semenov, V.D. Krevchik, Y. Wang, Chem. Eng. J. 358 (2019) 30.
[36] Y. Wei, K. Li, Z. Cheng, M. Liu, H. Xiao, P. Dang, S. Liang, Z. Wu, H. Lian, J. Lin, Adv. Mater. 31 (2019) 1807592.
[37] Y. Li, Z.F. Shi, S. Li, L.Z. Lei, H.F. Ji, D. Wu, T.T. Xu, Y.T. Tian, X.J. Li, J. Mater. Chem. C 5 (2017) 8355.
[38] A. Clearfield, S.P. Pack, J. Inorg. Nucl. Chem. 37 (1975) 1283.
[39] A.O. Rajeh, L. Szirtes, J. Radioanal, Nucl. Chem. 214 (1999) 83.
[40] S.E. Horsley, D.V. Nowell, D.T. Stewart, Spectrochim. Acta. A 30 (1974) 535.
[41] B.M. Mosby, A. Díaz, V. Bakhmutov, A. Clearfield, A.C.S. Appl, Mater. Interfaces 6 (2014) 585.
[42] A.S. Maria Chong, X.S. Zhao, J. Phys. Chem. B 107 (2003) 12650.
[43] O. Bixner, A. Lassenberger, D. Baurecht, E. Reimhult, Langmuir 31 (2015) 9198.
[44] L.M. Bronstein, X. Huang, J. Retrum, A. Schmucker, M. Pink, B.D. Stein, B. Dragnea, Chem. Mater. 19 (2007) 3624.
[45] F. Zhang, H. Zhong, C. Chen, X.G. Wu, X. Hu, H. Huang, J. Han, B. Zou, Y. Dong, ACS Nano 9 (2015) 4533.
[46] X. Di, Z. Hu, J. Jiang, M. He, L. Zhou, W. Xiang, X. Liang, Chem. Commun. 53 (2017) 11068.
[47] S. Jun, J. Lee, E. Jang, ACS Nano 7 (2013) 1472.
[48] S. Lou, T. Xuan, C. Yu, M. Cao, C. Xia, J. Wang, H. Li, J. Mater. Chem. C 5 (2017) 7431.
[49] W. Lv, L. Li, M. Xu, J. Hong, X. Tang, L. Xu, Y. Wu, R. Zhu, R. Chen, W. Huang, Adv. Mater. 31 (2019) 1900682.
[50] J.A. Christians, P.A. Miranda Herrera, P.V. Kamat, J. Am. Chem. Soc. 137 (2015) 1530.
[51] E. Mosconi, J.M. Azpiroz, F. De Angelis, Chem. Mater. 27 (2015) 4885.
[52] S. Huang, Z. Li, B. Wang, N. Zhu, C. Zhang, L. Kong, Q. Zhang, A. Shan, L. Li, A.C.S. Appl, Mater. Interfaces 9 (2017) 7249.
[53] T.Z. Ren, Z.Y. Yuan, B.L. Su, Chem. Commun. (2004) 2730.
[54] Q.R. Zhang, W. Du, B.C. Pan, B.J. Pan, W.M. Zhang, Q.J. Zhang, Z.W. Xu, Q.X. Zhang, J. Hazard. Mater. 152 (2008) 469.
[55] B.T. Diroll, G. Nedelcu, M.V. Kovalenko, R.D. Schaller, Adv. Funct. Mater. 27 (2017) 1606075.
[56] S.N. Habisreutinger, T. Leijtens, G.E. Eperon, S.D. Stranks, R.J. Nicholas, H.J. Snaith, Nano Lett. 14 (2014) 5561.
[57] S. Liu, G. Shao, L. Ding, J. Liu, W. Xiang, X. Liang, Chem. Eng. J. 361 (2019) 937.
[58] H. Xu, J. Wang, T. Xuan, C. Lv, J. Hou, L. Zhang, Y. Dong, J. Shi, Chem. Eng. J. 364 (2019) 20.
[59] X. Di, L. Shen, J. Jiang, M. He, Y. Cheng, L. Zhou, X. Liang, W. Xiang, J. Alloy Compd. 729 (2017) 526.
[60] F. Zhang, Z.F. Shi, Z.Z. Ma, Y. Li, S. Li, D. Wu, T.T. Xu, X.J. Li, C.X. Shan, G.T. Du, Nanoscale 10 (2018) 20131.
[61] S. Li, Z. Shi, F. Zhang, L. Wang, Z. Ma, D. Yang, Z. Yao, D. Wu, T.T. Xu, Y. Tian, Y. Zhang, C. Shan, X.J. Li, Chem. Mater. 31 (2019) 3917.
[62] W. Chen, T. Shi, J. Du, Z. Zang, Z. Yao, M. Li, K. Sun, W. Hu, Y. Leng, X. Tang, A.C.S. Appl, Mater. Interfaces 10 (2018) 43978.
[63] A. Bhaumik, S. Inagaki, J. Am. Chem. Soc. 123 (2001) 691.
[64] G. Alberti, M. Casciola, U. Costantino, J. Colloid Interface Sci. 107 (1985) 256.
[65] E. Boccalon, M. Nocchetti, M. Pica, A. Romani, M. Casciola, Dalton Trans. 47 (2018) 2976.